Magnetic Resonance Imaging 57 (2019) 165–175

Contents lists available at ScienceDirect

Magnetic Resonance Imaging

journal homepage: www.elsevier.com/locate/mri

Original contribution

Robustly reconstructing magnetic resonance images via structure decomposition

Xiaomei Yang, Wen Xu, Ruisen Luo, Xiujuan Zheng*, Kai Liu

College of Electrical Engineering and Information Technology, Sichuan University, No.24 South Section 1, Yihuan Road, Chengdu, China

ARTICLE INFO

Keywords:
Structure decomposition
Second-degree total variation
Non-local total variation
Alternating minimization scheme
Magnetic resonance imaging

ABSTRACT

In magnetic resonance (MR) imaging, for highly under-sampled k-space data, it is typically difficult to reconstruct images and preserve their original texture simultaneously. The high-degree total variation (HDTV) regularization handles staircase effects but still blurs textures. On the other hand, the non-local TV (NLTV) regularization can preserve textures, but will introduce additional artifacts for highly-noised images. In this paper, we propose a reconstruction model derived from HDTV and NLTV for robust MRI reconstruction. First, an MR image is decomposed into a smooth component and a texture component. Second, for the smooth component with sharp edges, isotropic second-order TV is used to reduce staircase effects. For the texture component with piecewise constant background, NLTV and contourlet-based sparsity regularizations are employed to recover textures. The piecewise constant background in the texture component contributes to accurately detect non-local similar image patches and avoid artifacts introduced by NLTV. Finally, the proposed reconstruction model is solved through an alternating minimization scheme. The experimental results demonstrate that the proposed reconstruction model can effectively achieve satisfied quality of reconstruction for highly under-sampled k-space data.

1. Introduction

Under-sampled k-space data is desired to effectively speed up magnetic resonance (MR) imaging. However, under-sampled k-space data leads to aliasing artifacts in reconstructed MR images. Compressed sensing (CS) [1,2] has shown the great potential on eliminating aliasing artifacts and improving quality of reconstructed MR images [3]. Because the number of under-sampled k-space data is much fewer, CS-MR image reconstruction is a typical ill-posed inverse problem and could be effectively solved via regularization approaches. The regularization model for reconstructing MR images is

$$\min_{u}\left\{\frac{1}{2}\|y-\mathbf{A}u\|_2^2+\lambda\varphi(u)\right\}, \tag{1}$$

where $u\in\mathbb{C}^N$ is vectorized from a desired $\sqrt{N}\times\sqrt{N}$ MR image, $y\in\mathbb{C}^M$ is acquired measurement in k-space, the matrix $\mathbf{A}\in\mathbb{C}^{M\times N}(M<N)$ acts as an under-sampling Fourier operator, $\|\cdot\|_2$ denotes L_2 norm that enforces data fidelity between k-space measurement and reconstructed images, λ is a positive regularization parameter, and $\varphi(u)$ is the regularization introduced by sparse transform (e.g., wavelet [4], contourlet [5], shearlet [6,7], sparse dictionary learning [8]) or low-rank constraint[9,10].

Among sparse regularizations, total variation (TV) [4,11], playing as a sparsity of gradient, can robustly handle extremely sharp edges, while it cannot well preserve texture and tends to introduce severe staircase effects in the smooth regions of reconstructed images [12]. Recently, high-order derivative-based regularizations, e.g., high-degree total variation (HDTV) [13-15] and total generalized variation (TGV) [16], have been proposed to eliminate the staircase artifacts. However, a high-order term will blur texture [17,18].

In order to well preserve texture, non-local methods, including fractional-order TV (FOTV) [18,19] and non-local TV (NLTV) regularizations [12,20-23], have been proposed. However, if NLTV regularization is used as the only constraint for inverse problems, when similar image patches cannot be accurately detected, NLTV causes blocky artifacts [21]. The performance of FOTV regularization depends on the selection of fractional order of differentiation. However, a fractional order is difficult to be simultaneously tuned for both smooth regions and textures [24]. The hybrid models, e.g. FOTV combined with sparse transform [18], TV combined with HDTV [25-27], NLTV [28], have been proposed to improve quality of reconstructed MR images. However, these methods globally process images without considering special features, e.g. smooth regions and textures [29].

In this paper, by decomposing an MR image into a smooth

* Corresponding author.
E-mail address: xiujuanzheng@scu.edu.cn (X. Zheng).

https://doi.org/10.1016/j.mri.2018.11.020
Received 13 August 2018; Received in revised form 7 November 2018; Accepted 22 November 2018

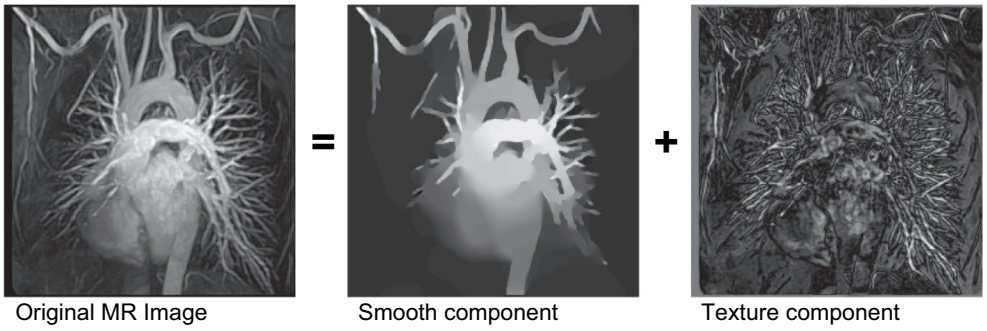

Fig. 1. Structure decomposition of MR image. (a) original MR image; (b) smooth component; (c) texture component.

component with sharp edges and a texture component with piecewise constant background [29], we apply different sparse regularizations to the two components, respectively, to solve the ill-posed inverse problem. For the smooth component, the isotropic second-order total variation (ISOTV) regularization is employed to reduce staircase effects and preserve sharp edges. For the texture component, first, NLTV regularization is used to preserve texture, since its piecewise constant background helps NLTV to accurately detect non-local similar image patches and suppress artifacts; and secondly, the contourlet-based [31-33] regularization is involved to further improve the quality of reconstructed images. We use the strategy of alternating minimization scheme to conquer subproblems one by one to finally reconstruct high-quality MR images for highly under-sampled k-space data. Experimental results verify the effectiveness of the proposed algorithm.

2. The proposed reconstruction model

As shown in Fig. 1, an MR image u can be decomposed into a smooth component u_s and a texture component u_t as [29]

$$u = u_s + u_t, \tag{2}$$

where u_s and u_t are of sharp edge and piecewise constant background, respectively. In this paper, by applying ISOTV regularization to u_s as well as applying NLTV and contourlet-based sparsity regularizations to u_t, we propose a reconstruction model as

$$\min_{u_s,u_t}\left\{\frac{1}{2}\|\mathbf{A}(u_s+u_t)-y\|_2^2+\lambda\mathrm{ISOTV}(u_s)+\mu_1\mathrm{NLTV}(u_t)+\mu_2\|\Psi(u_t)\|_1\right\}, \tag{3}$$

where λ, μ_1 and μ_2 are positive regularization parameters, $\|\Psi(u_t)\|_1$, the L_1 norm of $\Psi(u_t)$, plays as the contourlet-based sparsity regularization for u_t.

2.1. ISOTV regularization for u_s

The ISOTV regularization of a continuous image f is defined as [13]

$$\begin{aligned}\mathrm{ISOTV}(f) &= \int_\Omega \sqrt{\frac{1}{2\pi}\int_0^{2\pi}|s_2^{\mathrm{T}}(\theta)g_2(x,y)|^2 d\theta}\,dxdy\\ &= \int_\Omega \sqrt{g_2^*(x,y)W^*Wg_2(x,y)}\,dxdy\\ &= \int_\Omega \|Wg_2(x,y)\|_2\,dxdy,\end{aligned} \tag{4}$$

with

$$s_2(\theta)=[\cos(\theta)^2,\ 2\sin(\theta)\cos(\theta),\ \sin(\theta)^2]^{\mathrm{T}},$$

$$g_2(x,y)=\left[\frac{\partial^2 f(x,y)}{\partial x^2},\ \frac{\partial^2 f(x,y)}{\partial x\partial y},\ \frac{\partial^2 f(x,y)}{\partial y^2}\right]^{\mathrm{T}} \tag{5}$$

and

$$W=\frac{1}{4}\begin{bmatrix}\sqrt{2}+1 & 0 & \sqrt{2}-1\\ 0 & 2\sqrt{2} & 0\\ \sqrt{2}-1 & 0 & \sqrt{2}+1\end{bmatrix},$$

where θ is the sampling angle [13], the symbol * denotes the conjugate transpose operation for a matrix, and W is the weighted matrix for $g_2(x,y)$. In discrete domain, the ISOTV regularization in Eq.(4) is given as

$$\mathrm{ISOTV}(u_s)=\|\mathbf{D}_2u_s\|_1=\sum_{i=1}^{N}\|\mathbf{D}_2u_s(i)\|_2, \tag{6}$$

where $\mathbf{D}_2$ is an operator of weighted second-order derivative and defined as

$$\begin{aligned}\mathbf{D}_2u_s(i) &= [\mathbf{D}_{2,xx}u_s(i),\ \mathbf{D}_{2,xy}u_s(i),\ \mathbf{D}_{2,yy}u_s(i)]^{\mathrm{T}}\\ &= W[u_{s,xx}(i),\ u_{s,xy}(i),\ u_{s,yy}(i)]^{\mathrm{T}},\end{aligned} \tag{7}$$

where $[u_{s,xx}(i),u_{s,xy}(i),u_{s,yy}(i)]^{\mathrm{T}}$ is the discrete form of Eq. (5) [13].

2.2. NLTV regularization and contourlet-based regularization for u_t

Given a pixel i in u_t, its nonlocal discrete gradient can be calculated by [20]

$$\mathbf{D}_{\mathrm{NL}}u_t(i,j)=(u_t(j)-u_t(i))\sqrt{w(u_t(i),u_t(j))} \tag{8}$$

with

$$w(u_t(i),u_t(j))=\exp\left\{-\frac{G_\sigma\otimes\|u_t(i+\cdot)-u_t(j+\cdot)\|^2}{2h^2}\right\}, \tag{9}$$

where j is a non-local pixel in the searching neighborhood window of i, G_σ is the Gaussian kernel with standard deviation σ, h is a non-local filtering parameter, $\otimes$ is a convolution operator, and '$\cdot$' in $u_t(i+\cdot)$ denotes a square patch centered at the pixel i. With the weight $w(u_t(i),u_t(j))$ measuring the similarity between two neighboring patches $u_t(i+\cdot)$ and $u_t(j+\cdot)$, we define the discrete NLTV regularization for u_t as [20]

$$\begin{aligned}\mathrm{NLTV}(u_t) &= \|\mathbf{D}_{\mathrm{NL}}u_t\|_1=\sum_{i=1}^{N}\|D_{\mathrm{NL}}u_t(i)\|_2\\ &= \sum_{i=1}^{N}\sqrt{\sum_{j=1}^{N_i}[u_t(i)-u_t(j)]^2w(u_t(i),u_t(j))},\end{aligned} \tag{10}$$

where N_i is the size of the searching neighborhood window of i.

In Eq. (3), $\|\Psi(u_t)\|_1$ is the contourlet-based sparsity regularization, and $\Psi(u_t)$ is contourlet transform (CLT) [31-33] used for multi-directional and multi-scale decomposition. With CLT, we can decompose u_t into several directional sub-bands at multi-scale to overcome the wavelet's disadvantage which only decomposes an image into three directions.

3. Alternating minimization algorithm for the proposed model

In this section, we present a scheme for solving the problem described by Eq. (3). By replacing ISOTV(u_s) and NLTV(u_t) with Eqs. (6) and (10), respectively, we can rewrite Eq. (3) as

$$\min_{u_s,u_t}\left\{\frac{1}{2}\|\mathbf{A}(u_s+u_t)-y\|_2^2+\lambda\|\mathbf{D}_2u_s\|_1+\mu_1\|\mathbf{D}_{\mathrm{NL}}u_t\|_1+\mu_2\|\Psi(u_t)\|_1\right\}, \tag{11}$$

which is a non-linear multi-parameter optimization problem. To solve Eq. (11), we use the alternating minimization scheme [34] as follows:

1. Initialize

$$u^{(0)}=\mathbf{A}^{\mathrm{H}}y \tag{12}$$

$$u_s^{(0)}=\mathrm{L_0Smoothing}(u^{(0)}) \tag{13}$$

$$u_t^{(0)}=u^{(0)}-u_s^{(0)} \tag{14}$$

where $\mathbf{A}^{\mathrm{H}}$ is the adjoint operator of $\mathbf{A}$, and $\mathrm{L_0Smoothing}(u^{(0)})$ is to implement L_0 gradient minimization (15) defined as [35]

$$u_s^{(0)}=\arg\min_{u_s^{(0)}}\{\|u_s^{(0)}-u^{(0)}\|_2^2+\lambda_s\|\nabla u_s^{(0)}\|_0\}, \tag{15}$$

where λ_s is a non-negative parameter, the term $\nabla u_s^{(0)}$ is the gradient of $u_s^{(0)}$, and $\|\nabla u_s^{(0)}\|_0$ is the smooth term defined as the L_0 norm of $\nabla u_s^{(0)}$.

2. At $(k+1)^{th}$ iteration, $u_s^{(k+1)}$ and $u_t^{(k+1)}$, the approximates of u_s and u_t, are calculated by

$$u_s^{(k+1)}=\arg\min_{u_s}\left\{\frac{1}{2}\|\mathbf{A}(u_s+u_t^{(k)})-y\|_2^2+\lambda\|\mathbf{D}_2u_s\|_1\right\} \tag{16}$$

and

$$u_t^{(k+1)}=\arg\min_{u_t}\left\{\frac{1}{2}\|\mathbf{A}(u_s^{(k)}+u_t)-y\|_2^2+\mu_1\|\mathbf{D}_{\mathrm{NL}}u_t\|_1+\mu_2\|\Psi(u_t)\|_1\right\}, \tag{17}$$

respectively, and u is updated by

$$u^{(k+1)}=u_s^{(k+1)}+u_t^{(k+1)}. \tag{18}$$

3. When $u^{(k+1)}$ converges, the iterations stop and the final u is obtained.

3.1. Solving the problem (16) for u_s

The half-quadratic splitting minimization strategy [34] is employed to conveniently solve the problem (16) for u_s. By introducing an auxiliary variable b as $b=\mathbf{D}_2u_s$, we can convert the problem (16) into

$$(u_s,b)=\arg\min_{u_s,b}\left\{\frac{1}{2}\|\mathbf{A}(u_s+u_t^{(k)})-y\|_2^2+\lambda\|b\|_1\right\}\text{s.t.}b=\mathbf{D}_2u_s, \tag{19}$$

and then, by using Augmented Lagrangian, we finally have an unconstraint form of the problem (19) as

$$(u_s,b)=\arg\min_{u_s,b}\left\{\frac{1}{2}\|\mathbf{A}(u_s+u_t^{(k)})-y\|_2^2+\lambda\left(\|b\|_1+\frac{\beta}{2}\|\mathbf{D}_2u_s-b\|_2^2\right)\right\}, \tag{20}$$

where the penalty parameter β [34], initially taking a small value, is gradually increased in order to speed up the convergence of Eq. (20).

By using the alternating minimization strategy again, we divide the problem (20) into two subproblems as

$$b^{(k+1)}=\arg\min_b\left\{\|b\|_1+\frac{\beta}{2}\|\mathbf{D}_2u_s^{(k)}-b\|_2^2\right\} \tag{21}$$

and

$$u_s^{(k+1)}=\arg\min_{u_s}\left\{\frac{1}{2}\|\mathbf{A}(u_s+u_t^{(k)})-y\|_2^2+\frac{\lambda\beta}{2}\|\mathbf{D}_2u_s-b^{(k+1)}\|_2^2\right\}, \tag{22}$$

and we conquer them one by one as follows.

For Eq. (21), through multi-dimensional shrinkage formula [13], we have its explicit solution as

$$b^{(k+1)}=(b_{xx}^{(k+1)},b_{xy}^{(k+1)},b_{yy}^{(k+1)}), \tag{23}$$

with

$$\begin{cases}b_{xx}^{(k+1)}(i)=\mathrm{shrink_M}\left(\mathbf{D}_{2,xx}u_s^{(k)}(i),\frac{1}{\beta},|\mathbf{D}_2u_s^{(k)}(i)|\right)\\ b_{xy}^{(k+1)}(i)=\mathrm{shrink_M}\left(\mathbf{D}_{2,xy}u_s^{(k)}(i),\frac{1}{\beta},|\mathbf{D}_2u_s^{(k)}(i)|\right),\\ b_{yy}^{(k+1)}(i)=\mathrm{shrink_M}\left(\mathbf{D}_{2,yy}u_s^{(k)}(i),\frac{1}{\beta},|\mathbf{D}_2u_s^{(k)}(i)|\right)\end{cases}$$

where

$$|\mathbf{D}_2u_s^{(k)}(i)|=\sqrt{(\mathbf{D}_{2,xx}u_s^{(k)}(i))^2+(\mathbf{D}_{2,xy}u_s^{(k)}(i))^2+(\mathbf{D}_{2,yy}u_s^{(k)}(i))^2}$$

and

$$\mathrm{shrink_M}(s,\tau,z)=\mathrm{sign}(s)\max(z-\tau,0)\frac{s}{z}. \tag{24}$$

Then for the subproblem (22), by differentiating each term with respect to u_s and setting the derivative to zero, we can obtain

$$\mathbf{A}^{\mathrm{T}}(\mathbf{A}(u_s+u_t^{(k)})-y)+\lambda\beta(\mathbf{D}_2)^{\mathrm{T}}(\mathbf{D}_2u_s-b^{(k+1)})=0. \tag{25}$$

Under the period boundary conditions for u_s, $\mathbf{A}^{\mathrm{T}}\mathbf{A}$ and $\mathbf{D}_2^{\mathrm{T}}\mathbf{D}_2$ with circulant blocks structure can be diagonalized by DFT, and thus we can efficiently solve the subproblem (22) by

$$u_s^{(k+1)}=\mathcal{F}^{-1}\left(\frac{\mathcal{F}(\mathbf{A}^{\mathrm{T}}(y-\mathbf{A}u_t^{(k)})+\lambda\beta(\mathbf{D}_2)^{\mathrm{T}}b^{(k+1)})}{\mathcal{F}(\mathbf{A}^{\mathrm{T}}\mathbf{A})+\lambda\beta\mathcal{F}((\mathbf{D}_2)^{\mathrm{T}}\mathbf{D}_2)}\right), \tag{26}$$

where $\mathcal{F}$ and $\mathcal{F}^{-1}$ denote DFT and inverse DFT operators, respectively, and $\left(\frac{\cdot}{\cdot}\right)$ denotes an element-wise division.

3.2. Solving the problem (17) for u_t

By using the gradient descent, we can obtain the proximal map v_t of u_t at each iteration through

$$v_t^{(k+1)}=u_t^{(k)}+\rho\mathbf{A}^{\mathrm{T}}(y-A(u_s^{(k+1)}+u_t^{(k)})), \tag{27}$$

where ρ is a positive step. Then, we convert Eq. (17) into a de-noising problem as

$$u_t^{(k+1)} = \arg\min_{u_t} \left\{ \frac{1}{2} \|v_t^{(k+1)} - u_t\|_2^2 + \mu_1 \|\mathbf{D}_{\mathrm{NL}} u_t\|_1 + \mu_2 \|\Psi(u_t)\|_1 \right\}. \tag{28}$$

Next, we use composite splitting algorithms [36] to decompose Eq. (28) into two simpler regularization subproblems as

$$u_{t,1}^{(k+1)} = \arg\min_{u_t} \left\{ \frac{1}{2\rho} \|v_t^{(k+1)} - u_t\|_2^2 + 2\mu_1 \|\mathbf{D}_{\mathrm{NL}} u_t\|_1 \right\} \tag{29}$$

and

$$u_{t,2}^{(k+1)} = \arg\min_{u_t} \left\{ \frac{1}{2\rho} \|v_t^{(k+1)} - u_t\|_2^2 + 2\mu_2 \|\Psi(u_t)\|_1 \right\}. \tag{30}$$

The subproblem (29) is a traditional NLTV denoising problem, and can be approximately solved by using the split Bregman NLTV(SBNLTV) algorithm [21]. However, it is time-consuming to calculate the similarity weight w in Eq. (9) for SBNLTV. In this case, SBNLTV is modified to update the similarity weight every P iteration to reduce the computational time. The experiences demonstrate that $P = 5$ will be acceptable to accelerate the algorithm. The subproblem (30) is solved by using, in the CLT domain [33], soft iterative thresholding defined as

$$u_{t,2} = \Psi^{-1}\left(\max\left(\left| \Psi\left(v_t^{(k+1)} \right) \right| - 2\rho\mu_2, 0 \right) \right), \tag{31}$$

where Ψ^{-1} is inverse CLT. Finally, we solve u_t of Eq. (17) by

$$u_t = \frac{1}{2}(u_{t,1} + u_{t,2}), \tag{32}$$

where $u_{t,1}$ and $u_{t,2}$ are the solutions of Eqs. (29) and (30), respectively.

In summary, the whole work flow of solving Eq. (11) is described in Algorithm 1, which involves two loops. The outer loop increases β, and the inner loop computes b, u_s, u_t with a fixed β.

Algorithm 1. Algorithm for MRI reconstruction in Eq. (11).

Input:

Given a measured y,

- Set λ, μ, β, δ, stopping criterion ϵ, and two maximum loops K_1 and K_2
- Initialize $u_s^{(0)}$ and $u_t^{(0)}$ via (13) and (14)

Iteration:

for $n = 1, 2, \ldots, K_1$ **do**
  for $k = 1, 2, \ldots, K_2$ **do**
    Compute b via (23);
    Compute u_s via (26);
    Compute v_t via (27);
    Compute $u_t = \frac{1}{2}(u_{t,1} + u_{t,2})$, where $u_{t,1}$ and $u_{t,2}$ are obtained by using SBNLTV and (31), respectively;
    Compute $u = u_s + u_t$;
    if $\|u^{(k+1)} - u^{(k)}\|_2^2 / \|u^{(k)}\|_2^2 \le \epsilon$ **then**
      break;
    end if
    Update β via $\beta = \beta A_{cc}$.
  end for
end for

A_{cc} (> 1) is a constant.

4. Results

We evaluate the proposed reconstruction model over highly undersampled k-space data generated from four MR images (heart, brain, chest and artery, as shown in Fig. 2) [1], and the four original MR images are used as the ground truth. For the purpose of convenient comparisons, we resize the images into 256 × 256, and normalize the intensity into [0,1]. Variable-density under-sampling method [4,13], as shown in Fig. 3, is used to acquire y in Eq. (11). The sampling ratio is defined as M/N. Signal-to-noise ratio (SNR) [13] and the structural similarity index (SSIM) [37] are adopted to evaluate the quality of reconstructed images. SNR is defined as

$$\mathrm{SNR} = -10\log_{10}\left(\frac{\|u_{\mathrm{o}} - u_{\mathrm{r}}\|_2^2}{\|u_{\mathrm{o}}\|_2^2} \right), \tag{33}$$

where u_{o} and u_{r} are the original images and reconstructed images, respectively. SSIM is defined as

$$\mathrm{SSIM} = \frac{(2\eta_{u_{\mathrm{r}}}\eta_{u_{\mathrm{o}}} + C_1)(2\sigma_{u_{\mathrm{r}},u_{\mathrm{o}}} + C_2)}{(\eta_{u_{\mathrm{r}}}^2 + \eta_{u_{\mathrm{o}}}^2 + C_1)(\sigma_{u_{\mathrm{r}}}^2 + \sigma_{u_{\mathrm{o}}}^2 + C_2)} \tag{34}$$

where $\eta_{u_{\mathrm{r}}}$ and $\eta_{u_{\mathrm{o}}}$ are the mean intensity of u_{r} and u_{o}, $\sigma_{u_{\mathrm{r}}}^2$ and $\sigma_{u_{\mathrm{o}}}^2$ are deviation, $\sigma_{u_{\mathrm{r}},u_{\mathrm{o}}}$ represents the covariance between u_{r} and u_{o}, and C_1 and C_2 are two constants to avoid instability. The SSIM ranges in [0,1]. Higher SNR and higher SSIM stand for higher reconstructed quality.

4.1. Comparisons

We compare the proposed reconstruction model with other state-of-the-art methods, i.e. NLTV [21], HDTV [13], NLTV-FCSA [23], WaTMRI [38], and PANO [22]. Note that NLTV-FCSA uses both NLTV regularization and a wavelet-based sparsity regularization; WaTMRI joints wavelet tree sparsity and TV regularization; and PANO uses patch-based nonlocal operator to sparsify MR images. Meanwhile, PANO provides two reconstruction models PANO-Under and PANO-Full, whose difference is whether to use a guide image from under-sampled data or fully-sampled data.

We obtained the codes of other 6 methods from the authors' websites for fair comparisons. For the proposed reconstruction model, we set the parameters as: the regularization parameters $\lambda = 6.5 \times 10^{-5}$ and $\mu_1 = \mu_2 = 10^{-2}$, the initial value of the penalty parameter $\beta = 150$, the penalty acceleration factor $A_{cc} = 1.5$, the step size $\rho = 0.25$, and the stopping tolerance $\varepsilon = 10^{-8}$. When using SBNLTV algorithm to solve $u_{t,1}$ in Eq. (29), we set the sizes of pixel patches and searching neighborhood window as 5×5 and 15×15, then select 20 neighboring patches with the best similarity. In addition, we set the maximum number of iterations to 500 as that in WaTMRI and NLTV-FCSA, and run 150 iterations to guarantee its convergence for NLTV. In HDTV and the proposed reconstruction model, we set the maximum numbers of outer- and inner-iterations as 10 and 15, respectively, i.e., $K_1 = 10$ and $K_2 = 15$ in Algorithm 1.

For the generated noise-free under-sampled k-space data with sampling ratio varying from 10% to 40%, we reconstruct the MR images by using the proposed method as well as the other 6 methods, and list the results of SNRs and SSIMs in Table 1. It is shown that PANO-Full achieves the best performance by incorporating prior information (patch similarity) learned from fully sampled image. However, PANO-Full cannot work well for undersampled k-space data well due to lack of prior information from ground truth. So that, PANO-Under can be used instead of PANO-Full to learn similarity from a guide image estimated from the under-sampled measurements. As shown in Table 1, the proposed method performs much better than PANO-Under, especially for highly under-sampled data.

[1] http://ranger.uta.edu/huang/R_StructuredSparsity.htm

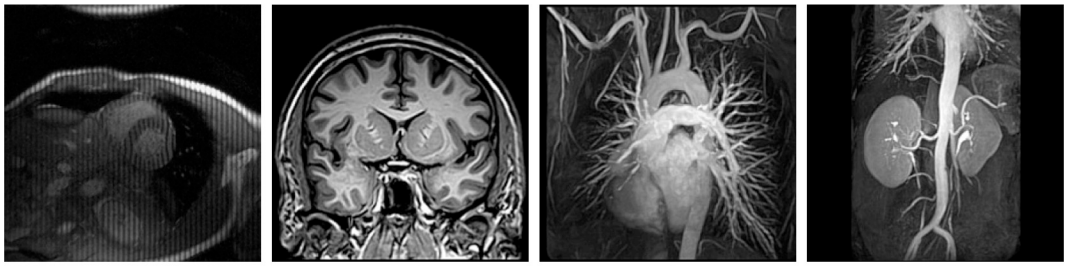

Fig. 2. Four ground-truth MR images. (a) Heart, (b) brain, (c) chest, and (d) artery.

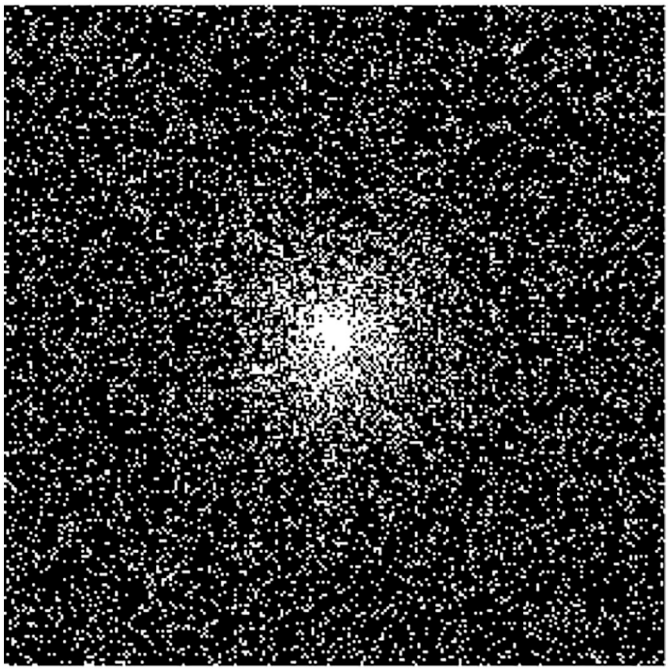

Fig. 3. Variable-density under-sampling pattern, with 15% sampling ratio.

Next, we add complex Gaussian noise to y with the noising signal-to-noise ratio (NSNR) of 30 dB. NSNR is defined as $\text{NSNR} = 10\log_{10}(\sigma_y^2/\sigma_n^2)$, where σ_y^2 and σ_n^2 are the deviations of y and the added Gaussian noise, respectively. We vary the sampling ratio from 10% to 40%, and reconstruct MR images using all 7 methods. In Table 2, the results demonstrated that the proposed method outperformed the others in most cases.

In order to further evaluate our method, instead of complex Gaussian noise, we add Rician noise [39] with deviation $\sigma_n = 10$ to ground-truth u and then under-sample k-space data to have measurement data y. With Rician-noised and under-sampled y, we reconstruct MR images by using all 7 methods again. As shown in Table 3, SNRs and SSIMs are all decreased compared with the Gaussian-noised data. Although NLTV shows the largest SNRs especially for high sampling ratio, SSIMs of NLTV are the smallest in most cases. On the contrary, our proposed reconstruction model shows more balanced performance.

For the Gaussian- or Rician-noised y sampled with ratio of 15%, the residues of the reconstructed images are shown in Figs. 4–7. The residues of the proposed reconstruction model demonstrate more randomly distributed errors, while the residues of the other methods show more profile patterns.

4.2. Discussions of λ and $\mu_{1,2}$

In the proposed reconstruction model, the regularization parameters, λ, μ_1 and μ_2, are used to balance the contributions of ISOTV regularization, NLTV and contourlet regularization. Although different μ_1 and μ_2 might achieve better performance, we hypothesize $\mu_1 = \mu_2$ to reduce computational complexity for reconstructing MRI. The values of λ and $\mu_{1,2}$ are selected from a set of candidates, to gain the satisfied SNR value for "heart" image. After that, the selected parameters λ and $\mu_{1,2}$ are transferred to reconstruct other images.

At first, we acquired Gaussian-noised under-sampled k-space data at 15% sampling ratio with 30 dB-NSNR. With varying λ over $[6.5\times10^{-7}, 6.5\times10^{-6}, 1.0\times10^{-5}, 6.5\times10^{-5}, 1.0\times10^{-4}, 6.5\times10^{-3}]$, fixing $\mu_{1,2}$ to 1.0×10^{-2}, and keeping the other parameters as the same as those in the Section 4.1, we illuminate the changes of SNR values for the reconstructed images in Fig. 8 (a). From the results, it is found that the performance of the proposed reconstruction model is less affected by λ when $\lambda < 1.0\times10^{-4}$, otherwise the increase of λ could lead to the worse performance. Taking "heart" image as an example, with $\lambda = 6.5\times10^{-5}$ and 6.5×10^{-4}, we show error images between the ground-truth and reconstructed images (the 1st column), the reconstructed texture images (the 2nd column), and the reconstructed smooth region with sharp edges (the 3rd column) in Fig. 9. From the reconstructed texture images in Fig. 9 (b), it is found that the noise and artifacts around edges cannot be effectively suppressed for $\lambda = 6.5\times10^{-4}$. To achieve higher SNRs, λ could be set at the range of

Table 1
With no additive noise, the results of SNR (dB) and SSIM (SNR/SSIM) of NLTV, HDTV, NLTV-FCSA, WatMRI, PANO-Under, PANO-Full, and our proposed reconstruction model for different sampling rates. (Red color indicates the best performance, blue color indicate the second best performance.)

MRI	Sampling ratio	10%	15%	20%	25%	30%	35%	40%
Heart	NLTV	15.06/0.4187	16.43/0.4707	15.85/0.4387	16.68/0.4595	18.40/0.5141	18.34/0.4769	18.90/0.4896
	HDTV	16.76/0.5944	19.67/0.7397	18.53/0.6774	19.68/0.7246	23.10/0.8150	24.18/0.8203	26.17/0.8400
	NLTV-FCSA	15.56 /0.6829	17.72/0.7648	17.28/0.7496	18.66/0.7711	21.05/0.8440	22.44/0.8672	24.11/0.8984
	WaTMRI	16.63/0.6945	19.38/0.8084	18.38/0.7632	19.89/0.7937	22.55/0.8704	23.69/0.8861	25.46/0.9161
	PANO-Under	17.34/0.6585	20.55/0.8026	19.07/0.7425	20.44/0.7891	24.24/0.8803	25.33/0.8925	26.98/0.9197
	PANO-Full	18.96/0.6836	22.68/0.8224	20.97/0.7768	23.16/0.8486	25.86/0.9017	26.98/0.9147	28.48/0.9359
	Proposed	18.81/0.6853	21.82/0.8144	20.58/0.7638	21.86/0.7900	25.07/0.8487	25.99/0.8609	27.60/0.8778
Brain	NLTV	NaN	16.94/0.6783	18.08/0.7081	19.05/0.7341	20.04/0.7522	20.80/0.7641	21.59/0.7772
	HDTV	14.46/0.6409	15.85/0.6850	17.63/0.7255	19.33/0.7542	21.34/0.7834	22.60/0.7960	24.82/0.8148
	NLTV-FCSA	15.51/0.7088	17.19/0.7447	18.78/0.7709	21.05/0.7985	23.44/0.8212	25.41/0.8338	27.90/0.8462
	WaTMRI	15.63/0.7146	17.33/0.7528	18.97/0.7786	21.18/0.8059	23.46/0.8251	25.37/0.8351	27.55/0.8447
	PANO-Under	16.95/0.7113	18.67/0.7482	20.34/0.7773	21.99/0.7955	24.10/0.8156	25.41/0.8234	27.68/0.8354
	PANO-Full	18.23/0.7409	19.65/0.7658	21.24/0.7901	22.81/0.8043	24.74/0.8205	26.04/0.8278	28.12/0.8379
	Proposed	16.12/0.6976	17.79/0.7356	19.64/0.7678	21.12/0.7866	23.13/0.8081	24.16/0.8154	25.60/0.8264
Chest	NLTV	17.75/0.5900	18.38/0.6155	19.17/0.6461	19.97/0.6737	20.67/0.6961	21.13/0.7101	21.77/0.7292
	HDTV	17.95/0.7371	18.87/0.7833	20.29/0.8201	22.06/0.8536	23.57/0.8849	24.85/0.8996	26.30/0.9219
	NLTV-FCSA	16.23/0.7120	16.88/0.7406	18.24/0.7780	19.41/0.8105	20.98/0.8467	22.11/0.8716	23.73/0.8953
	WaTMRI	16.85/0.7337	17.73/0.7729	19.21/0.8108	20.54/0.8428	22.26/0.8783	23.63/0.9021	25.07/0.9213
	PANO-Under	19.68/0.7939	21.00/0.8357	22.52/0.8714	23.87/0.8983	25.42/0.9239	26.76/0.9353	28.07/0.9510
	PANO-Full	20.78/0.8224	22.13/0.8615	23.53/0.8902	24.80/0.9129	26.22/0.9343	27.46/0.9442	28.74/0.9574
	Proposed	20.09/0.8002	21.15/0.8382	22.67/0.8706	24.21/0.8950	25.58/0.9203	26.63/0.9283	27.64/0.9459
Artery	NLTV	18.67/0.4042	19.64/0.4258	20.34/0.4419	20.97/0.4544	21.54/0.4733	21.97/0.4793	22.55/0.4908
	HDTV	20.05/0.5315	21.79/0.5616	23.45/0.5877	25.46/0.6122	27.35/0.6373	28.80/0.6473	30.66/0.6633
	NLTV-FCSA	19.65/0.5682	21.43/0.6030	22.98/0.6284	25.31/0.6565	27.28/0.6762	29.56/0.6931	31.89/0.7061
	WaTMRI	20.57/0.5955	22.71/0.6302	24.42/0.6501	26.61/0.6708	28.51/0.6846	30.22/0.6941	32.44/0.7046
	PANO-Under	22.48/0.5932	24.48/0.6199	26.10/0.6444	28.04/0.6648	29.54/0.6792	31.06/0.6881	33.28/0.7006
	PANO-Full	23.03/0.6006	24.80/0.6254	26.41/0.6474	28.24/0.6663	29.80/0.6819	31.28/0.6897	33.47/0.7011
	Proposed	23.14/0.5846	24.79/0.6099	26.01/0.6313	28.15/0.6519	29.11/0.6723	29.46/0.6771	29.91/0.6870

NaN*: Can't reconstruct MR image.

$[1.0 \times 10^{-5}, 1.0 \times 10^{-4}]$.

Similarly, by setting $\mu_{1,2}$ from 1.0×10^{-5} to 10 with a step size of 10, and fixing λ to 6.5×10^{-5}, the SNR values of the four reconstructed images based on the proposed reconstruction model are calculated and shown in Fig. 8 (b). From the results, it is shown that $\mu_{1,2}$ could significantly affect the performance of the proposed reconstruction model. When $\mu_{1,2} \leq 1.0 \times 10^{-2}$, the proposed reconstruction model is unable to achieve the satisfied SNR values. To pursue the higher SNRs, $\mu_{1,2}$ could be larger than 1.0×10^{-2}, while SNR values show the tendency of gradually declining with the increase of $\mu_{1,2}$.

For u, which is degraded by Rician noise with $\sigma_n = 5$, 10 and 15, and y, which is under-sampled from k-space data with ratio of 15%, we repeat similar experiments with the same settings as those for Gaussian data. For the proposed reconstruction model, taking the "brain" image as an example, the SNRs with different σ_n are plotted in Fig. 10. It is shown that the range of λ for better SNRs is similar to those of Gaussian-

Table 2
With additive complex Gaussian noise (NSNR = 30 dB) to y, the results of SNR (dB) and SSIM (SNR/SSIM) of NLTV, HDTV, NLTV-FCSA, WatMRI, PANO-Under, PANO-Full, and our proposed method for different sampling rates. (Red color indicates the best performance and blue color indicates the second best performance.)

MRI	Sampling ratio	10%	15%	20%	25%	30%	35%	40%
Heart	NLTV	15.04/0.4187	16.39/0.4707	15.84/0.4387	16.62/0.4595	18.37/0.5141	18.33/0.4769	18.87/0.4896
	HDTV	16.55/0.5974	19.36/0.7434	18.24/0.6851	19.37/0.7310	22.43/0.8238	23.35/0.8312	24.97/0.8558
	NLTV-FCSA	14.83/0.6742	16.56/0.7335	16.20/0.7297	17.42/0.7540	19.01/0.8028	19.94/0.8274	20.91/0.8504
	WaTMRI	15.35/0.6904	17.28/0.7734	16.77/0.7520	17.95/0.7756	19.61/0.8296	20.37/0.8466	21.39/0.8728
	PANO-Under	16.20/0.6472	18.38/0.7846	17.56/0.7272	18.78/0.7655	21.15/0.8558	21.68/0.8634	22.59/0.8944
	PANO-Full	17.35/0.6874	19.75/0.8132	18.92/0.7671	20.33/0.8222	21.96/0.8800	22.45/0.8875	23.12/0.9091
	Proposed	18.66/0.6863	21.38/0.8143	20.11/0.7678	21.20/0.7875	23.71/0.8778	24.21/0.8926	25.21/0.9195
Brain	NLTV	NaN	16.91/0.6783	17.88/0.7081	18.84//0.7341	19.86/0.7522	20.62//0.7641	21.36/0.7772
	HDTV	14.45/0.6412	15.79/0.6835	17.48/0.7235	19.04/0.7514	20.81/0.7796	21.91/0.7914	23.68/0.8092
	NLTV-FCSA	14.38/0.6889	15.59/0.7227	16.64/0.7450	17.86/0.7695	18.64/0.7821	19.04/0.7915	19.30/0.7982
	WaTMRI	14.43/0.6950	15.59/0.7318	16.62/0.7490	17.85/0.7756	18.83/0.7899	19.50/0.7991	20.05/0.8061
	PANO-Under	15.69/0.6850	17.03/0.7219	18.22/0.7479	19.36/0.7710	20.62/0.7895	21.41/0.7992	22.41/0.8104
	PANO-Full	16.75/0.7129	17.81/0.7393	18.92/0.7625	19.93/0.7808	20.99/0.7953	21.76/0.8033	22.66/0.8130
	Proposed	16.17/0.6961	17.63/0.7339	19.23/0.7640	20.38/0.7817	21.99/0.8022	22.67/0.8071	23.61/0.8172
Chest	NLTV	17.52/0.5901	18.28/0.6155	19.11/0.646	19.86/0.6737	20.52/0.6961	21.03/0.7101	21.63/0.7292
	HDTV	17.89/0.7352	18.66/0.7820	20.10/0.8177	21.63/0.8505	22.96/0.8811	24.01/0.8968	25.13/0.9175
	NLTV-FCSA	15.28/0.6834	15.78/0.7108	16.82/0.7411	17.68/0.7739	18.69/0.8016	19.37/0.8222	20.25/0.8419
	WaTMRI	15.56/0.7029	16.08/0.7283	17.11/0.7650	18.00/0.7953	19.01/0.8244	19.76/0.8450	20.56/0.8621
	PANO-Under	17.87/0.7857	18.83/0.7968	19.82/0.8331	20.72/0.8572	21.66/0.8843	22.32/0.8986	23.02/0.9155
	PANO-Full	18.67/0.7857	19.57/0.8230	20.54/0.8530	21.30/0.8749	22.11/0.8958	22.66/0.9083	23.27/0.9229
	Proposed	19.90/0.7968	20.82/0.8331	22.07/0.8631	23.16/0.8845	24.04/0.9066	24.63/0.9144	25.19/0.9264
Artery	NLTV	18.45/0.4042	19.52/0.4258	20.28/ 0.4419	20.91/0.4544	21.43/0.4733	21.89/0.4793	22.46/0.4908
	HDTV	19.76/0.5321	21.33/0.5624	22.66/0.5884	24.34/0.6119	25.78/0.6354	26.77/0.6437	28.04/0.6609
	NLTV-FCSA	16.98/0.4941	17.77/0.5203	18.37/0.5333	19.03/0.5534	19.25/0.5600	19.62/0.5706	19.99/0.5847
	WaTMRI	17.22/0.5134	18.04/0.5379	18.88/0.5603	19.58/0.5750	20.19/0.5855	20.79/0.5974	21.42/0.6112
	PANO-Under	19.41/0.5566	20.57/0.5830	21.49/0.6025	22.33/0.6178	22.92/0.6315	23.51/0.6405	24.11/0.6501
	PANO-Full	19.81/0.5646	20.86/0.5900	21.69/0.6084	22.52/0.6223	23.07/0.6349	23.63/0.6431	24.22/0.6520
	Proposed	22.77/0.5950	24.11/0.6204	24.96/0.6378	25.71/0.6523	26.13/0.6638	26.24/0.6685	26.41/0.6729

NaN*: Can't reconstruct MR image.

noised data, while smaller/larger $\mu_{1,2}$ achieves higher SNRs for smaller/larger σ_n. The tendency of SSIMs is similar with that of SNRs. Finally, by comprehensively considering Gaussian and Rician noises, we set $\mu_{1,2} \in [1.0 \times 10^{-3}, 1.0 \times 10^{-2}]$. In the future, we will study on an adaptive method to automatically select the values of λ and $\mu_{1,2}$.

4.3. The convergence

Convergence is an important characteristic performance for image reconstruction. In this experiment, we investigate the convergence of the proposed reconstruction model by trading off iterations and SNRs. For the "heart" image at sampling ratios of 10%, we obtain SNR sequence for NLTV, HDTV, NLTV-FCSA, and the proposed methods. Since PANO-Under and PANO-Full only provide pcoded files (content-obscured, and executable files), we cannot record SNR values at each iteration for these two methods. For under-sampled k-space data corrupted by complex Gaussian noise with 30 dB-NSNR, and the magnitude image corrupted by Rician noise with $\sigma_n = 10$, SNRs versus

Table 3
With additive Rician noise ($\sigma_n = 10$) to MR magnitude image u, the results of SNR (dB) and SSIM (SNR/SSIM) of NLTV, HDTV, NLTV-FCSA, WatMRI, PANO-Under, PANO-Full, and our proposed method for different sampling rates. (Red color indicates the best performance and blue color indicates the second best performance.)

MRI	Sampling ratio	10%	15%	20%	25%	30%	35%	40%
Heart	NLTV	13.35/0.3564	14.22/0.3932	13.89/0.3672	14.42/0.3858	15.17/0.425	15.21/0.4113	15.41/0.4236
	HDTV	13.59/0.5895	14.16/0.6592	13.52/0.6374	13.58/0.6455	14.20/0.6722	14.09/0.6701	14.14/0.6756
	NLTV-FCSA	12.45/0.4683	13.16/0.5496	13.07/0.5274	13.47/0.5573	14.07/0.6285	14.25/0.6185	14.48/0.6418
	WatMRI	13.25/0.6139	13.80/0.6633	13.21/0.6417	13.35/0.6464	13.68/0.6648	13.64/0.6636	13.65/0.6683
	PANO-UNder	13.75/0.6035	14.43/0.6791	13.79/0.6547	13.86/0.6688	14.14/0.6950	13.97/0.6913	13.89/0.6888
	PANO-Full	14.43/0.6506	14.92/0.7255	14.17/0.6937	14.34/0.7136	14.34/0.7202	14.11/0.7080	13.96/0.6987
	Proposed	14.20/0.6097	15.17/0.6835	14.47/0.6608	14.84/0.6701	15.28/0.6901	15.24/0.6894	15.29/0.6849
Brain	NLTV	NaN	15.47/0.6364	16.31/0.6657	16.99/0.6881	17.64/0.7086	18.08/0.7219	18.51/0.7329
	HDTV	13.41/0.6096	14.02/0.6494	14.93/0.6781	15.55/0.7044	16.49/0.7278	16.96/0.7373	17.52/0.7533
	NLTV-FCSA	12.33/0.5853	13.07/0.6121	13.82/0.6382	14.52/0.6647	15.34/0.6909	15.83/0.7051	16.42/0.7232
	WatMRI	12.99/0.6338	13.82/0.6692	14.64/0.6915	15.41/0.7177	16.34/0.7390	16.68/0.7459	17.22/0.7606
	PANO-UNder	13.89/0.6295	15.21/0.6802	15.26/0.7002	15.63/0.7199	16.31/0.7437	15.99/0.7449	16.97/0.7635
	PANO-Full	14.60/0.6566	15.73/0.6986	15.61/0.7140	15.89/0.7294	16.47/0.7494	16.11/0.7500	17.05/0.7661
	Proposed	13.73/0.6660	14.75/0.7046	15.81/0.7295	16.51/0.7482	17.54/0.7654	17.89/0.7689	18.38/0.7780
Chest	NLTV	16.95/0.5611	17.52/0.5909	18.19/0.6135	18.73/0.6425	19.40/0.6696	19.69/0.6755	20.14/0.7007
	HDTV	16.53/0.7050	16.28/0.7237	16.97/0.7384	17.57/0.7614	17.92/0.7752	18.30/0.7925	18.57/0.7968
	NLTV-FCSA	15.34/0.6202	15.87/0.6488	16.54/0.6746	17.11/0.7004	17.69/0.7224	18.13/0.7398	18.57/0.7578
	WatMRI	15.80/0.6983	16.19/0.7275	16.80/0.7489	17.27/0.7702	17.74/0.7880	17.99/0.7998	18.18/0.8064
	PANO-UNder	17.21/0.7357	17.75/0.7789	18.19/0.8024	18.21/0.8189	17.67/0.8291	17.83/0.8343	18.64/0.8402
	PANO-Full	17.81/0.7616	18.33/0.8034	18.61/0.8211	18.52/0.8316	17.84/0.8385	17.94/0.8408	18.75/0.8453
	Proposed	17.19/0.7596	17.67/0.7881	18.32/0.8017	18.81/0.8155	19.27/0.8255	19.48/0.8273	19.69/0.8308
Artery	NLTV	16.01/0.3842	16.51/0.4043	16.88/0.4182	17.09/0.4282	17.42/0.4489	17.56/0.4579	17.71/0.4669
	HDTV	15.94/0.5088	15.97/0.5227	16.10/0.5337	16.40/0.5445	16.51/0.5460	16.60/0.5509	16.66/0.5570
	NLTV-FCSA	14.52/0.4278	15.01/0.4504	15.43/0.4745	15.85/0.4888	16.11/0.5046	16.41/0.5188	16.66/0.5327
	WatMRI	15.54/0.5144	15.83/0.5296	16.05/0.5422	16.27/0.5500	16.31/0.5536	16.38/0.5584	16.37/0.5598
	PANO-UNder	15.69/0.5264	16.09/0.5503	16.61/0.5695	15.62/0.5638	15.97/0.5741	15.31/0.5739	15.89/0.5769
	PANO-Full	15.85/0.5386	16.22/0.5597	16.70/0.5758	15.72/0.5735	16.05/0.5782	15.35/0.5771	15.92/0.5788
	Proposed	16.53/0.5539	16.87/0.5660	17.08/0.5732	17.31/0.5776	17.42/0.5805	17.39/0.5746	17.43/0.5718

NaN*: Can't reconstruct MR image.

iterations is plotted in Fig. 11 (a) and (b), respectively. The results show that the proposed reconstruction model converges as the other methods but with higher SNRs.

5. Conclusions

In this paper, we propose an MRI reconstruction model by decomposing an MR image into a smooth component and a texture component, and then apply ISOTV, and integrated NLTV and contourlet regularization to these two components, respectively. We solve the proposed reconstruction model by using an alternating minimization scheme. Different MR images are employed in experiments to illustrate that the proposed reconstruction model can achieve the high-quality reconstructed images. Moreover, the results also indicate that the proposed reconstruction model can effectively suppress the artifact and preserve edges for lower sampling ratios. With NLTV regularization, the

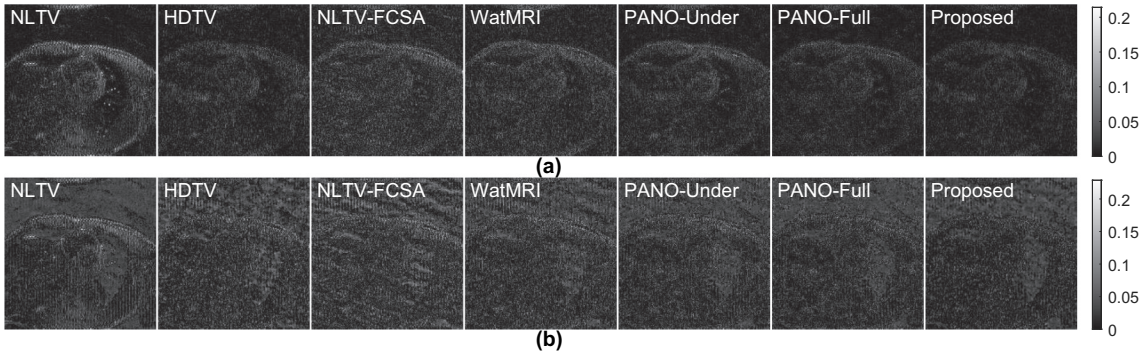

Fig. 4. Residues of the reconstructed "heart" images from noisy under-sampled k-space data with 15% sampling ratio. (a) Gaussian noise with 30 dB-NSNR in under-sampled k-space data; (b) Rician noise with $\sigma_n = 10$ in MR magnitude image.

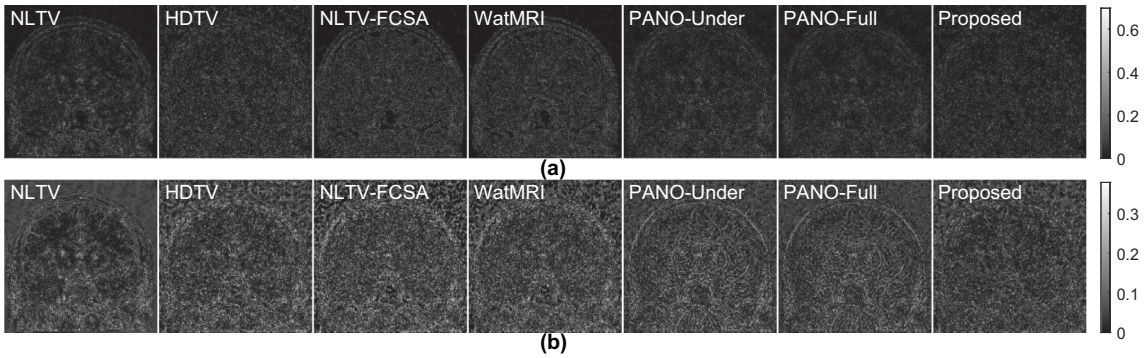

Fig. 5. Residues of the reconstructed "brain" images from noisy under-sampled k-space data with 15% sampling ratio. (a) Gaussian noise with 30 dB-NSNR in under-sampled k-space data; (b) Rician noise with $\sigma_n = 10$ in MR magnitude image.

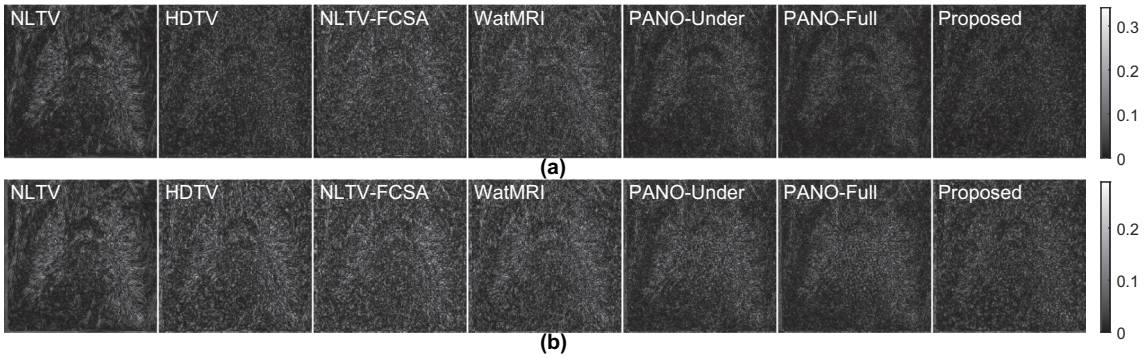

Fig. 6. Residues of the reconstructed "chest" images from noisy under-sampled k-space data with 15% sampling ratio. (a) Gaussian noise with 30 dB-NSNR in under-sampled k-space data; (b) Rician noise with $\sigma_n = 10$ in MR magnitude image.

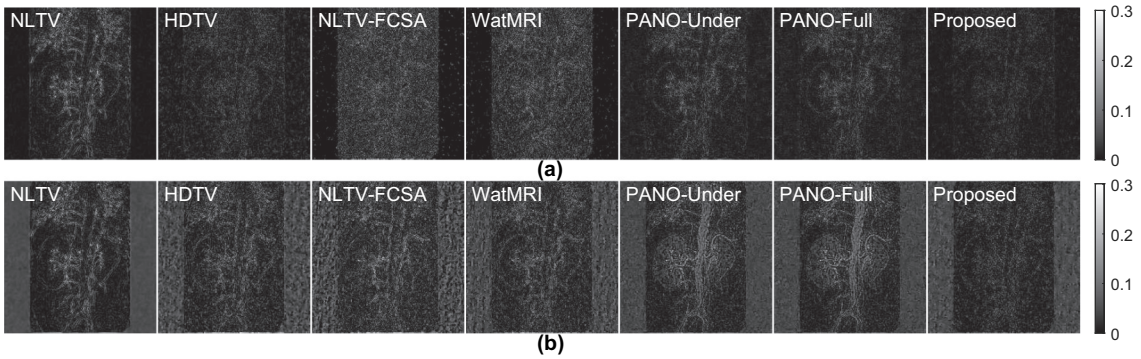

Fig. 7. Residues of the reconstructed "artery" images from noisy under-sampled k-space data with 15% sampling ratio. (a) Gaussian noise with 30 dB-NSNR in under-sampled k-space data; (b) Rician noise with $\sigma_n = 10$ in MR magnitude image.

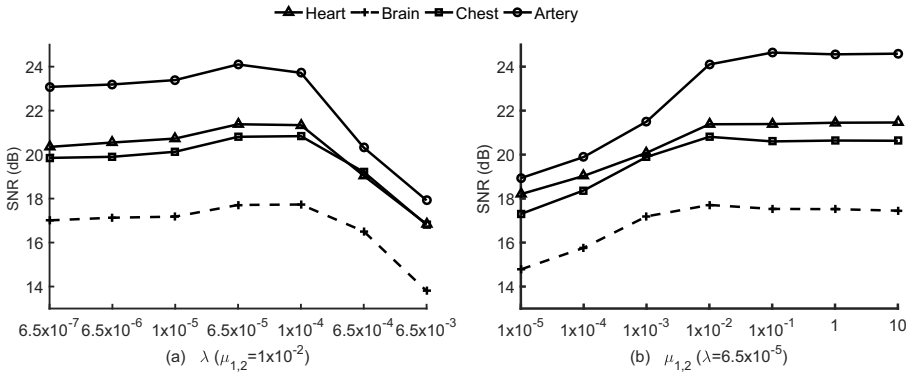

Fig. 8. SNR values with different regularization parameters λ and $\mu_{1,2}$, where complex Gaussian noise with 30 dB-NSNR is added in under-sampled k-space data of "heart" images. (a) Different λ (fixed $\mu_{1,2} = 1 \times 10^{-2}$), (b) different $\mu_{1,2}$($\mu_1 = \mu_2$, fixed $\lambda = 6.5 \times 10^{-5}$).

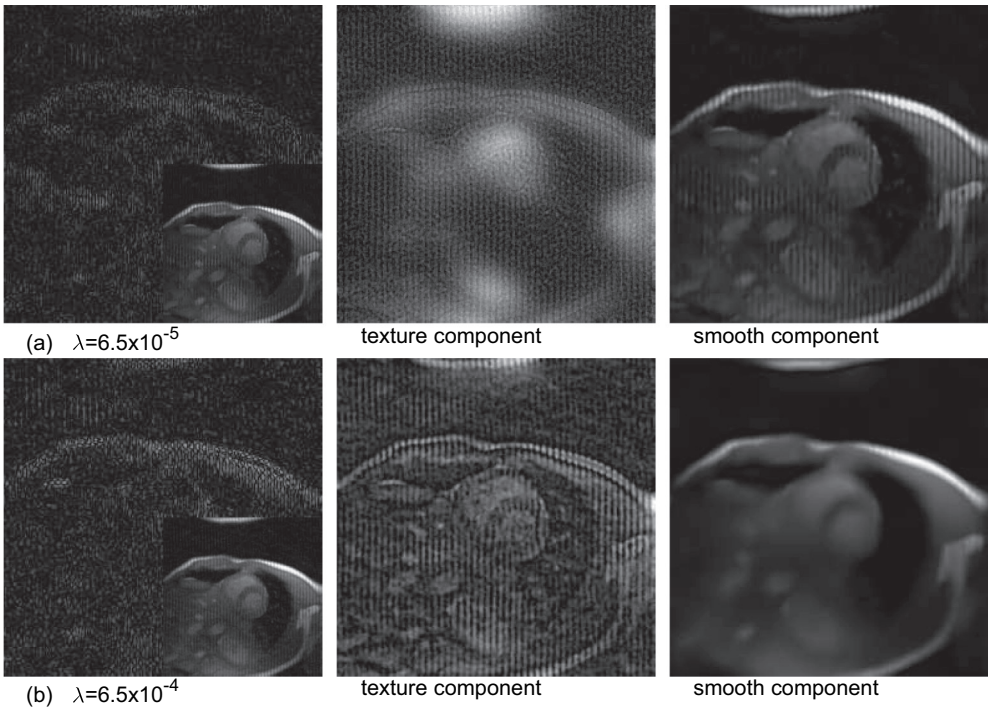

Fig. 9. Error images, reconstructed texture components and smooth components for "heart" images, with different regularization parameter λ and fixed $\mu_{1,2} = 1.0 \times 10^{-2}$. (a) $\lambda = 6.5 \times 10^{-5}$ (21.38 dB), (b) $\lambda = 6.5 \times 10^{-4}$ (19.04 dB).

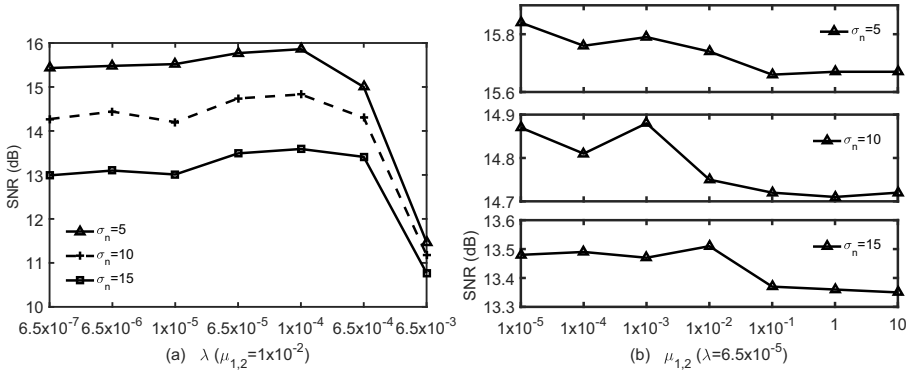

Fig. 10. SNR values with different regularization parameters λ and $\mu_{1,2}$, where Rician noise with different σ_n is added to "brain" magnitude images and then k-space is under-sampled. (a) Different λ (fixed $\mu_{1,2} = 1 \times 10^{-2}$), (b) different $\mu_{1,2}$($\mu_1 = \mu_2$, fixed $\lambda = 6.5 \times 10^{-5}$).

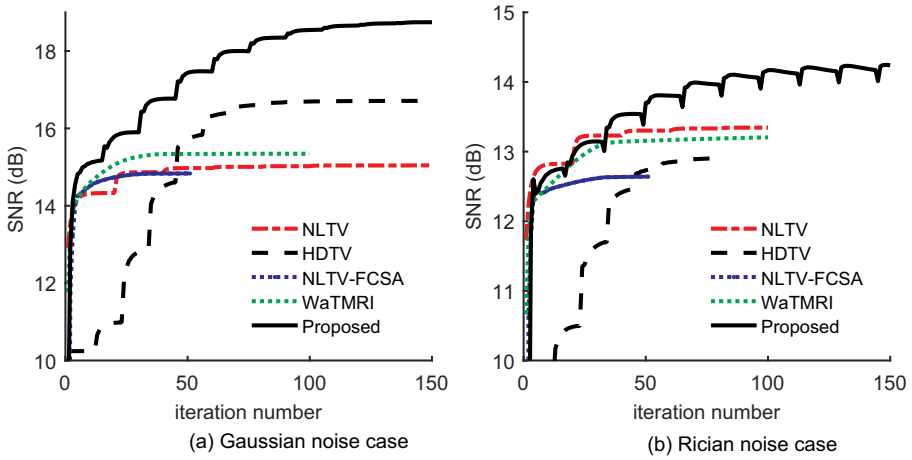

Fig. 11. Relation between SNR values and the iterations for 10% sampling ratio. (a) Gaussian noise case, (b) Rician noise case.

proposed method suffers from longer computation. The acceleration of the proposed method will be studied in the future.

References

[1] Donoho D L. Compressed sensing. IEEE Trans Inf Theory 2006;52(4):1289–306.
[2] Cands E J, Romberg J, Tao T. Robust uncertainty principles: exact signal reconstruction from highly incomplete frequency information. IEEE Trans Inf Theory 2006;52(2):489–509.
[3] Lustig M, Donoho D L, Santos J M, Pauly J M. Compressed sensing MRI. IEEE Signal Process Mag 2008;25(2):72–82.
[4] Michael L, Donoho D L, Pauly J M. Sparse MRI: the application of compressed sensing for rapid mr imaging. Magn Reson Med 2007;58(6):1182–95.
[5] Eslahi N, Aghagolzadeh A. Compressive sensing image restoration using adaptive curvelet thresholding and nonlocal sparse regularization. IEEE Trans Image Process 2016;25(7):3126–40.
[6] Huang Y, Paisley J, Lin Q. Bayesian nonparametric dictionary learning for compressed sensing MRI. IEEE Trans Image Process 2014;23(12):5007–19.
[7] Pejoski S, Kafedziski V, Gleich D. Compressed sensing MRI using discrete nonseparable shearlet transform and FISTA. IEEE Signal Process Lett 2015;22(10):1566–70.
[8] Zhan Z, Cai J, Guo D, Liu Y, Chen Z, Qu X. Fast multiclass dictionaries learning with geometrical directions in MRI reconstruction. IEEE Trans Biomed Eng 2016;63(9):1850–61.
[9] Hong M, Yu Y, Wang H, Liu F, Crozier S. Compressed sensing MRI with singular value decomposition based sparsity basis. Phys Med Biol 2011;56(19):6311–25.
[10] Lingala S G, Hu Y, DiBella E, Jacob M. Accelerated dynamic MRI exploiting sparsity and low-rank structure: k-t SLR. IEEE Trans Med Imaging 2011;30(5):1042–54.
[11] Block K T, Uecker M, Frahm J. Undersampled radial MRI with multiple coils. Iterative image reconstruction using a total variation constraint. Magn Reson Med 2007;57(6). 1086C–1098.
[12] Liu X, Huang L. A new nonlocal total variation regularization algorithm for image denoising. Math Comput Simul 2014;97. 224C–233.
[13] Hu Y, Jacob M. Higher degree total variation (HDTV) regularization for image recovery. IEEE Trans Image Process 2012;21(5):2559–71.
[14] Chan T, Marquina A, Mulet P. High-order total variation-based image restoration. SIAM J Sci Comput 2012;22(2). 503C–516.
[15] Liu P, Xiao L, Zhang J. Fast second degree total variation method for image compressive sensing. Plos One 2015;10(9):e0137115.
[16] Knoll F, Bredies K, Pock T, Stollberger R. Second order total generalized variation (TGV) for MRI. Magn Reson Med 2011;65(2):480–91.
[17] Lysaker M, Osher S, Tai X. Noise removal using smoothed normals and surface fitting. IEEE Trans Image Process 2004;13(10). 1345–C1357.
[18] Chen G, Zhang J, Li D. Fractional-order total variation combined with sparsifying transforms for compressive sensing sparse image reconstruction. J Vis Commun Image Represent 2016;38:407–22.
[19] Ren Z, He C, Zhang Q. Fractional order total variation regularization for image super-resolution. Signal Process 2013;93(9):2408–21.
[20] Gilboa G, Osher S. Nonlocal operators with applications to image processing. Siam J Multiscale Model Simul 2008;7(3):1005–28.
[21] Zhang X, Burger M, Bresson X. Bregmanized nonlocal regularization for deconvolution and sparse reconstruction. SIAM J Imag Sci 2010;3(3):253–76.
[22] Qu X, Hou Y, Lam aG Fan, Zhong J, Chen Z. Magnetic resonance image reconstruction from undersampled measurements using a patch-based nonlocal operator. Med Image Anal 2014;18(6):843–56.
[23] Huang J, Yang F. Compressed magnetic resonance imaging based on wavelet sparsity and nonlocal total variation. IEEE Int Symp Biomed Imaging 2012;5(1):968–71.
[24] Zhang J, Wei Z, Xiao L. Fractional-order iterative regularization method for total variation based image denoising. J Electron Imaging 2012;21(4):255–62.
[25] Feng C, Xiao L, Wei Z. Combined first- and second-order variational model for image compressive sensing. Math Probl Eng 2013;2013(3):206–26.
[26] Papafitsoros K, Schonlieb C. A combined first and second order variational approach for image reconstruction. J Math Imaging Vision 2014;48(2):308–38.
[27] Oh S, Woo H, Yun S, Kang M. Non-convex hybrid total variation for image denoising. J Vis Commun Image Represent 2013;24(3):332–44.
[28] Tang S, Gong W, Li W, Wang W. Non-blind image deblurring method by local and nonlocal total variation models. Signal Process 2014;94(1):339–49.
[29] Zhang J, Wei Z, Xiao L. Bi-component decomposition based hybrid regularization method for partly-textured CS-MR image reconstruction. Signal Process 2016;128:274–90.
[31] Chen L, Zhao J. Robust contourlet-based blind watermarking for depth-image-based rendering 3D images. Signal Process Image Commun 2017;54:56–65.
[32] Do M N, Vetterli1 M. The contourlet transform: an efficient directional multiresolution image representation. IEEE Trans Image Process 2005;14(12):2091–106.
[33] Qu X, Zhang W, Guo D, Cai C, Cai S, Chen Z. Iterative thresholding compressed sensing MRI based on contourlet transform. Inverse Prob Sci Eng 2010;18(6):737–58.
[34] Wang Yilun YJ, Wotao Y. A new alternating minimization algorithm for total variation image reconstruction. Inverse Prob Sci Eng 2008;1(3):248–72.
[35] Xu L, Lu C, Xu Y, Jia J. Image smoothing via L0 gradient minimization. ACM Trans Graph 2011;30(6):61–4.
[36] Huang J, Zhang S, Li H, Metaxas D. Composite splitting algorithms for convex optimization. Comput Vis Image Underst 2011;115(12):1610–22.
[37] Wang Z, Bovik A C, Sheikh H R, Simoncelli E P. Image quality assessment: from error visibility to structural similarity. IEEE Trans Image Process 2004;13(4):600–12.
[38] Chen C, Huang J. The benefit of tree sparsity in accelerated MRI. Med Image Anal 2014;18(6):834–42.
[39] Gudbjartsson H, Patz S. The Rician distribution of noisy MRI data. Magn Reson Med 1995;34(6):910–4.